

Structure of Arp2/3 Complex in Its Activated State and in Actin Filament Branch Junctions

Niels Volkmann,¹ Kurt J. Amann,² Svetla Stoilova-McPhie,¹
 Coumaran Egile,³ Dirk C. Winter,³ Larnelle Hazelwood,¹
 John E. Heuser,⁴ Rong Li,³ Thomas D. Pollard,² Dorit Hanein^{1*}

The seven-subunit Arp2/3 complex choreographs the formation of branched actin networks at the leading edge of migrating cells. When activated by Wiskott-Aldrich Syndrome protein (WASp), the Arp2/3 complex initiates actin filament branches from the sides of existing filaments. Electron cryomicroscopy and three-dimensional reconstruction of *Acanthamoeba castellanii* and *Saccharomyces cerevisiae* Arp2/3 complexes bound to the WASp carboxy-terminal domain reveal asymmetric, oblate ellipsoids. Image analysis of actin branches indicates that the complex binds the side of the mother filament, and Arp2 and Arp3 (for actin-related protein) are the first two subunits of the daughter filament. Comparison to the actin-free, WASp-activated complexes suggests that branch initiation involves large-scale structural rearrangements within Arp2/3.

The Arp2/3 complex is the cellular factor that generates new filaments in a site-directed, signal-controlled fashion at the leading edge of motile cells (1) and forms identical branches in vitro (2). The complex binds the sides and slow-growing (pointed) ends of actin filaments (3). The dendritic actin networks generated by the Arp2/3 complex have been thought to be critical for producing the force that drives lamellipodia protrusion. Conserved among eukaryotes, this seven-subunit complex consists of two actin-related proteins, Arp2 and Arp3, and five novel proteins. Structural models of the Arps (4) suggested that the complex provides a nucleation site for a new actin filament. The COOH-terminal region of WASp family members containing the WASp homology 2 (W) and acidic (A) domains, together with preassembled actin filaments, activates the Arp2/3 complex, thus promoting barbed (fast-growing) end nucleation of new (daughter) filaments (5–8). Electron microscopy, chemical cross-linking, yeast genetics, sedimentation, and hydrodynamic modeling provided evidence for the organization of the complex and identified subunits that interact with actin, WA, and profilin [reviewed in (9)]. Crystallography has not yet provided direct information on the structure of the complex. We used electron cryomicroscopy and single-particle analysis

to obtain the structure of WA-bound Arp2/3 complex at 3.2 nm resolution. Image analysis of actin filament branches formed by the Arp2/3 complex suggests that the Arps form the first two subunits in the daughter filament. A large conformational change, involving one of the Arps and at least one small subunit, appears to occur during branch formation.

Unstained, fully hydrated *Acanthamoeba* Arp2/3 complex bound to the WA domain of Scar, a WASp-like protein, was imaged in vitrified buffer (Fig. 1A) (10). Three independent three-dimensional (3D) reconstructions were calculated (11), and the high similarity among these reconstructions (>92% correlation) verified the reliability of the structure. The 0.5 Fourier shell correlation criterion (12) indicates a resolution of 3.2 nm (Fig. 1C). Gold labeling was used to localize the NH₂-terminus of WA within the reconstruction (13). Single-particle analysis of *Acanthamoeba* Arp2/3 complex without the WA domain bound did not converge to a consistent 3D reconstruction. It is conceivable that the WA domain stabilizes the free complex and locks it into a narrow range of conformations.

Saccharomyces cerevisiae Arp2/3 complex bound to the WA domain of yeast Bee1, a member of the WASp family, was imaged in uranyl acetate stain after air-drying (Fig. 1A) (14). Processing of this yeast data set converged to a 3D reconstruction similar to the *Acanthamoeba* structure (Fig. 1D). The Fourier shell correlation indicates a resolution of about 3.9 nm for the yeast reconstruction (Fig. 1C). The correlation between the yeast and the *Acanthamoeba* structures at 3.9 nm resolution is 90%. Thus, at this resolu-

tion, the complexes are nearly identical as anticipated from the conserved sequences of their subunits.

When contoured at a threshold containing 100% of the molecular mass (220 kD), WA-bound Arp2/3 complexes are oblate ellipsoids with dimensions of 13 nm by 9 nm by 5 nm (Fig. 1D). Contouring at a higher threshold reveals a region of lower density between two large lobes, giving the reconstructions a horseshoe shape. This is similar to images of shadowed complexes, which indicate a cleft between two domains of the complex (2, 15).

Electron cryomicroscopy was used to image frozen-hydrated actin filament branches produced by *Acanthamoeba* Arp2/3 complex activated by Scar-WA (16). Individual actin monomers and extra density at branch sites were clearly visible in filtered images (Fig. 2A). From the unfiltered images, 167 branches were selected and used to generate a two-dimensional (2D) image of the projection view. This 2D reconstruction clearly reveals subunits in both actin filaments (Fig. 2B) and is fully compatible with quick-frozen, deep-etched, rotary-shadowed samples of the same preparation (Fig. 2, C and D). Fourier-space analysis suggests a resolution of ~2.8 nm for the branch reconstruction. Myosin decoration of the branches formed by the yeast Arp2/3 complex in the presence of Bee1-WA (17) verified that the pointed ends of both filaments are directed toward the branch (Fig. 2E), as they are in extracted cells (18). This confirms that Arp2/3 complex nucleates actin filaments that grow at their barbed ends (2). In the 2D reconstruction, the mother filament continues unaffected through the branch, and an analysis of the diffraction pattern of the mother filament alone shows an undisturbed helical actin symmetry. These two findings indicate that the Arp2/3 complex is not inserted into the mother filament. The helical structure of the daughter filament starts about 6 nm from the side of the mother filament. Three bridges of density connect the pointed end of the daughter filament to three actin subunits in the mother filament. The density distribution in the connecting region indicates a thickness of about 5 nm. The quick-frozen, shadowed samples provide evidence that the contact occurs slightly out of plane (Fig. 2, C and D).

The helical symmetry of actin filaments and their defined polarity allowed us to fit atomic models of actin (19) unambiguously into the 2D reconstruction of both the mother and daughter filaments (Fig. 3A). If one assumes that all of the subunits of the mother and daughter filaments are actin, the remaining projection density at the branch junction is insufficient to accommodate the entire Arp2/3 complex. On the other hand, if two of the filament subunits are Arps [as postulated (20)], the complete complex can be accom-

¹The Burnham Institute, La Jolla, CA 92037, USA.

²Structural Biology Laboratory, Salk Institute for Biological Studies, La Jolla, CA 92037, USA. ³Department of Cell Biology, Harvard Medical School, Boston, MA 02115, USA. ⁴Department of Cell Biology, Washington University, School of Medicine, St. Louis, MO 63110, USA.

*To whom correspondence should be addressed. E-mail: dorit@burnham.org

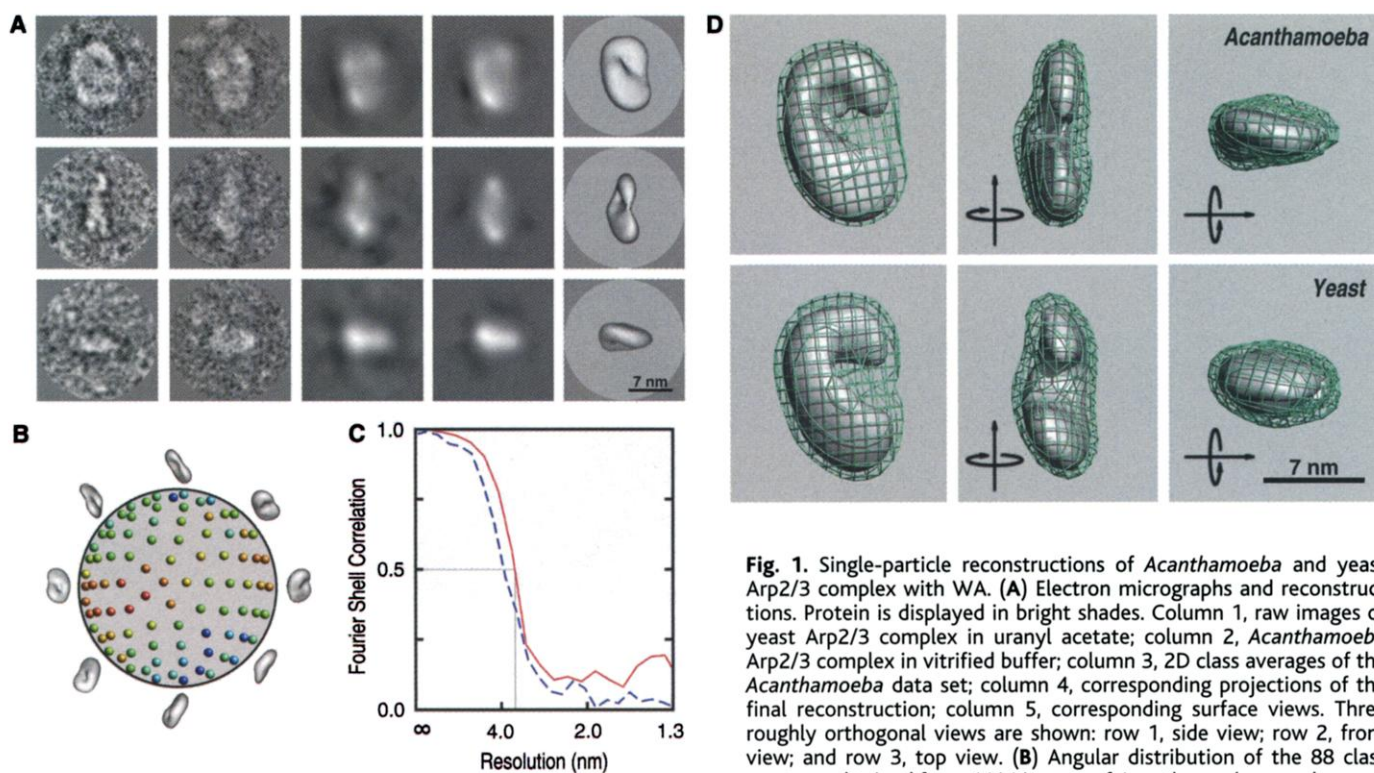


Fig. 1. Single-particle reconstructions of *Acanthamoeba* and yeast Arp2/3 complex with WA. (A) Electron micrographs and reconstructions. Protein is displayed in bright shades. Column 1, raw images of yeast Arp2/3 complex in uranyl acetate; column 2, *Acanthamoeba* Arp2/3 complex in vitrified buffer; column 3, 2D class averages of the *Acanthamoeba* data set; column 4, corresponding projections of the final reconstruction; column 5, corresponding surface views. Three roughly orthogonal views are shown: row 1, side view; row 2, front view; and row 3, top view. (B) Angular distribution of the 88 class averages obtained from 4414 images of *Acanthamoeba* complex used

to generate the 3D structure in the first row of (D). Surface views for some angles are shown for reference. Each class average is represented as a color-coded circle, where red corresponds to larger number of images contributing to the average (maximum 306) and blue corresponds to a low number of images (minimum 8). The diagram shows that the reconstruction is free of artifacts caused by missing views. (C) Fourier shell correlation between two reconstructions calculated from two randomly selected half sets of the respective data. Red is the *Acanthamoeba* data set, blue is yeast. (D) 3D reconstructions of *Acanthamoeba* (upper row) and yeast (lower row) Arp2/3 complex. The wire mesh isosurface (teal) encloses the complete molecular volume of the complex (relative molecular mass of 220 kD). The solid representation encloses 50% of the molecular mass. The three columns show views from the side (left column), front (middle column), and top (right column). The straight arrows indicate the axis and the circular arrows indicate the turning direction that generate a particular view from the side view (row 1).

modated within the volume. This is reasonable on structural grounds, because Arps share high sequence identity to actin and are about the same size as actin, thus are likely to be folded similarly (4). In our model (Fig. 3A), the Arps are the first two subunits of the daughter filament. The available structural data cannot distinguish whether Arp2 is at the pointed end of the daughter filament or in the second position. However, the pattern of conserved surface residues between actin and Arp2 (4) leads us to speculate that Arp2 makes the majority of contacts with actin at the growing, barbed end of the daughter filament and Arp3 is positioned at the pointed end of the branch (Fig. 3A). In this model, three subunits (p40, p35, and p14) of the complex make contact with subdomain 1 of actin subunits in the mother filament. This arrangement is fully consistent with previous cross-linking (2, 15), biochemical (8), and genetic (21) studies. After adding Arp2/3 complex to preformed actin filaments, we saw—in both frozen-hydrated and freeze-etched, quick-frozen samples—masses attached to the sides of the filaments whose size and shape (Fig. 3B) correspond very closely to those of the Arp2/3 complex model built from the 2D branch-junction reconstruc-

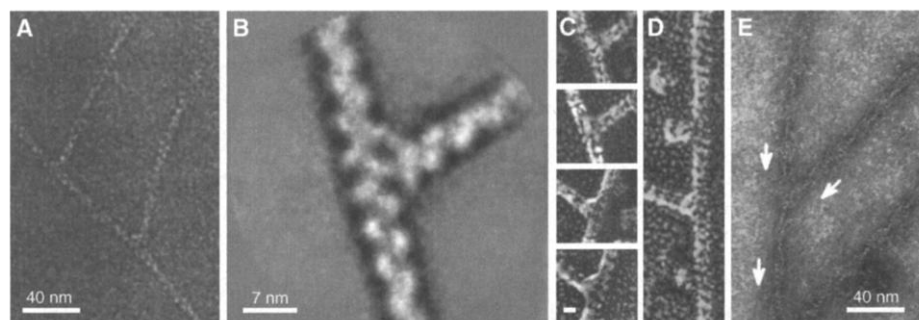


Fig. 2. Electron micrographs of actin filament branches mediated by Arp2/3 complex. (A) Frozen hydrated actin branches made by *Acanthamoeba* Arp2/3 complex. For visualization purposes, a Gaussian real-space filter was applied to the image. (B) 2D reconstruction using 167 images of actin filament branches. (C) A gallery of quick-frozen, deep-etched, rotary-shadowed actin branches mediated by *Acanthamoeba* Arp2/3 complex. Bar is 7 nm. Note that the daughter filament appears to be elevated in respect to the mother filament for branches pointing to the left (lower two) and on a lower plane than the mother filament when branches point to the right (upper two). (D) A quick-frozen, shadowed actin filament with a branch pointing to the left. Note the visibility of the 37.5-nm right-handed half-twist crossover repeats. (E) Negatively stained actin branches mediated by yeast Arp2/3 complex, decorated with expressed myosin catalytic domain (no light chains). The arrows follow the direction of the bound myosin heads that show the appearance of arrowheads indicating the polarity of the actin filaments.

tion (Fig. 3, A and C). Because the filaments were polymerized before addition of Arp2/3 complex, our observation of the complex bound to their sides is consistent with the hypothesis that branches form on the side of

mother filaments (22), and it does not support the hypothesis that one of the Arps is incorporated into the mother filament and the other into the daughter filament (23).

If the Arps form the first two subunits of

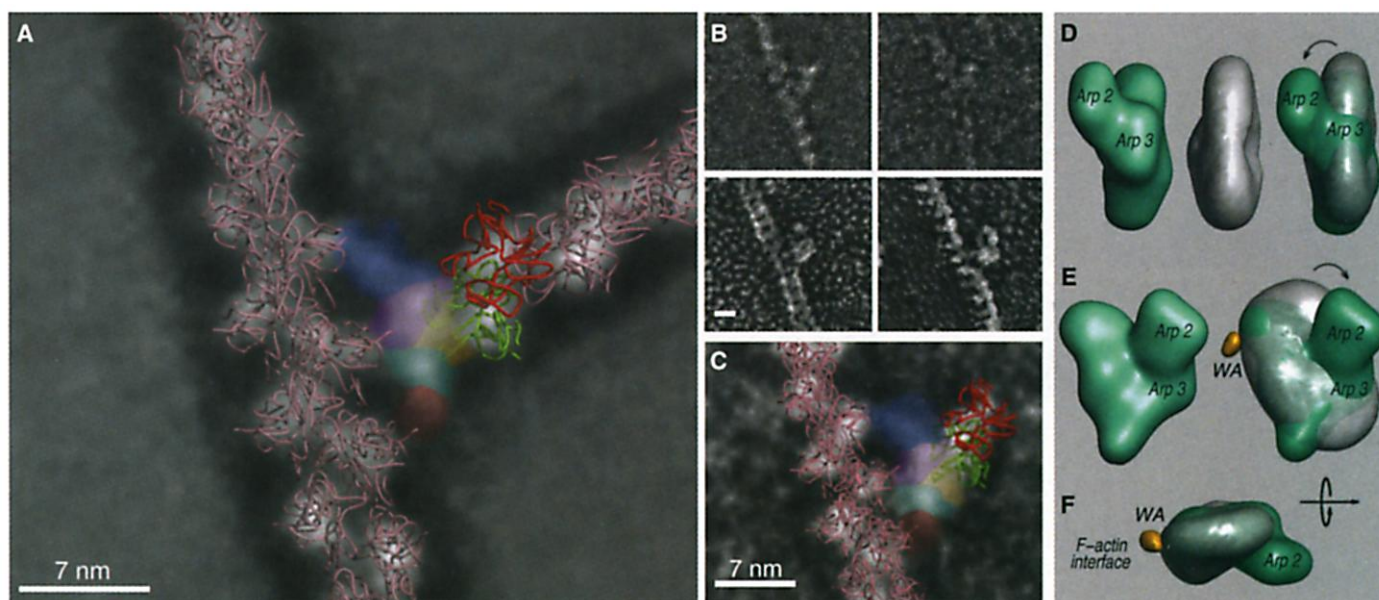


Fig. 3. Molecular model of the actin-bound Arp2/3 complex at the branch junction. **(A)** Model of actin filament branches mediated by *Acanthamoeba* Arp2/3 complex. The 2D reconstruction from Fig. 2B is shown in the background for reference. The backbone of the molecular model of filamentous actin, fitted to the 2D reconstruction, is shown in pink. The first two subunits of the daughter filament, shown in red and green backbone presentation, are assigned to be Arps. The other five subunits of the complex are assigned to the rest of the projection density using the proximity information from cross-linking, genetic, and yeast two-hybrid experiments [summarized in (9)]: p40 (purple); p35 (pink); p18 (yellow); p19 (light blue); p14 (orange). The size of the regions was chosen to approximate the respective molecular weights, assuming a thickness of about 5 nm. The barbed ends of the filaments are toward the top of the figure. **(B)** Images of Arp2/3 complex from *Acanthamoeba* bound to the side of mother filaments. All samples in the actin experiments were prepared in the presence of the activator (WA). Upper row: in vitrified buffer, a Gaussian real-space filter was applied to the images for visualization. Lower row: quick-frozen, deep-etched, rotary-shadowed specimen. Note the similarity of the position and shape of the complex to that seen at the branch junction shown in (A). Bar is 7 nm. **(C)** Average of six aligned images of Arp2/3 complex bound to the side of filaments in vitrified buffer overlaid with backbone presentation of an actin filament (pink) and backbone presentations of Arp2 (red) and Arp3 (green) in positions similar to those in (A). The remaining density was assigned to the other subunits and colored as in (A). **(D)** Density representations

of the models of actin-bound (green) and the free, WA-activated (as shown in Fig. 1D, gray) Arp2/3 complex. The density for the branched model was calculated using a filament-like configuration for the two Arps and using the remaining projection density assuming a thickness of ~5 nm. The view was generated by turning the model of the complex in (A) by 90° counter-clockwise. This view corresponds to the front view depicted in Fig. 1. On the right, the best fit of the density representing the branched model (green) into the 3D reconstruction of the free Arp2/3 complex (gray) is shown. Note that the density corresponding to Arp2 cannot be accommodated by the reconstruction of the free complex. A possible large-scale conformational change of the free, activated complex upon binding to actin, a rearrangement in the position of Arp2, is indicated by an arrow. **(E)** The density for the branched model (green, left) and the best fit (right) of the branched model density (green) into that of the free Arp2/3 complex (gray). The binding site of the WA NH₂-terminus (gold), as assigned by the labeling. With this fit the WA NH₂-terminus is in close proximity to the F-actin interface of the Arp2/3 complex. The orientation of this view matches that of the projection densities in (A) and (C) and corresponds to the side view depicted in Fig. 1. A possible rearrangement [as in (D)] of Arp2 upon binding to the filament is indicated by an arrow. **(F)** The best fit of the density of the branched model (green) into that of the free Arp2/3 complex (gray). WA NH₂-terminus is shown in gold. This view corresponds to the top view depicted in Fig. 1. The straight and circular arrows on the right indicate the axis and turning direction that generate this view from the view in (E) (the side view in Fig. 1).

the daughter filament and have the helical symmetry of actin filaments, the Arp2/3 complex must change shape during formation of the branch. The reason for this is that two Arps arranged along the genetic helix of the actin filament cannot fit into the planar structure of the free Arp2/3 complex (Fig. 3, D through F). Thus, at least one of the Arps must rearrange to fit into the projection view of the actin-bound structure. Although it is possible to postulate reasonable subunit rearrangements that are consistent with the available data, molecular details of this conformational change will require an atomic structure of the complex and additional analysis.

A conformational change coupled to branching nucleation is consistent with the observation that preformed actin filaments are secondary activators of nucleation (8, 20,

23–25). The reconstructions support the model (9) that activation of Arp2/3 involves rearrangement of the subunits in the complex to bring the Arps together in a filamentous arrangement. Interestingly, gold labeling places the WA domain close to the interface between the mother filament and Arp2/3 complex (Fig. 3, E and F), suggesting that WA and the mother filament may cooperate to facilitate the rearrangement of subunits in the complex, bringing the Arps together in a conformation suitable for barbed-end nucleation of the branch.

References and Notes

1. T. M. Svitkina, G. G. Borisy, *J. Cell Biol.* **145**, 1009 (1999).
2. R. D. Mullins, J. A. Heuser, T. D. Pollard, *Proc. Natl. Acad. Sci. U.S.A.* **95**, 6181 (1998).
3. R. D. Mullins, J. F. Kelleher, J. Xu, T. D. Pollard, *Mol. Biol. Cell* **9**, 841 (1998).

4. J. F. Kelleher, S. J. Atkinson, T. D. Pollard, *J. Cell Biol.* **131**, 385 (1995).
5. D. Yarar, W. To, A. Abo, M. D. Welch, *Curr. Biol.* **9**, 555 (1999).
6. R. Rohatgi et al., *Cell* **97**, 221 (1999).
7. C. Egile et al., *J. Cell Biol.* **146**, 1319 (1999).
8. L. M. Machesky et al., *Proc. Natl. Acad. Sci. U.S.A.* **96**, 3739 (1999).
9. R. D. Mullins, T. D. Pollard, *Curr. Opin. Struct. Biol.* **9**, 244 (1999).
10. *Acanthamoeba* Arp2/3 complex was purified by poly-L-proline (26) and gel filtration chromatography as described (22). Scar WA, the 65 COOH-terminal residues of human Scar1 protein (8), was expressed in bacteria from pMW172 (27) without induction and was purified as described (22). The preparations [buffer: 150 mM KCl, 10 mM Tris (pH 8.0), 100 μM CaCl₂, 200 μM ATP, 500 μM dithiothreitol (DTT)] were applied to copper grids coated with Quantifoil holey carbon films (Quantifoil Micro Tools GmbH, Jena, Germany) and plunged in liquid ethane. Images were obtained under low-dose conditions with the use of a Tecnai 12 electron microscope (FEI Electron Optics) and DH626 cryo-holder (Gatan, Inc.) at a nominal magnification of 67,000 at 2.5 μm defocus. The micrographs were digitized with a SCAI scanner

[Z(I Imaging Corporation, Englewood, CO)] with pixel size of 0.4 nm on the sample. Shadowed specimens were prepared as described (2). Handedness of the shadowed specimen was determined using the 5.1-nm left-handed actin repeat and the 37.5-nm right-handed half-twist crossover repeat, both visible in the images (Fig. 2D).

11. Image processing of single particles of *Acanthamoeba* Arp2/3 complex. Interactive selection from 46 images yielded 4414 particles (Fig. 1A). The particles were processed and analyzed using the EMAN (28) and COAN (29) software packages. A correction for the contrast transfer function was applied for all images. Absolute scaling was performed using the known helical symmetry of actin filaments present in the same images. For 3D reconstruction, particles were aligned to each other using the reference-free method, classified into 20 to 25 classes, and averaged. Briefly, particles that appear to be similar (by dot product) to one another were grouped together into a predefined number of groups, and then the particles within each group were mutually aligned and averaged. This generated a class average for each group that should represent one characteristic view of the particle. Several of these averages were then selected manually and passed to a Fourier common-lines routine that determines the relative orientations (Euler angles) of all selected averages, which are then combined to calculate an initial 3D model. This initial model was then iteratively refined against the data. Convergence was achieved when the Fourier shell correlation between successive iterations stabilized. Three independent starting models were generated from different subsets of the *Acanthamoeba* data set. Several rounds (15 to 25) of refinement were performed for each of these models using the complete data set. The three calculations converged to the same structure (Fig. 1D), as suggested by the high correlation values.
12. B. Böttcher, S. A. Wynne, R. A. Crowther, *Nature* **386**, 88 (1997).
13. Scar WA-Cys, containing a single cysteine residue at its NH₂-terminus, was purified as described (22) and then reacted with equimolar monoamino Nanogold (Nanoprobe) in 100 mM NaCl and 10 mM NaPO₄ (pH 7.0) for 16 hours at 4°C. Nanogold-labeled WA was further purified by 5-100 gel filtration chromatography in 100 mM NaCl, 10 mM Tris-HCl (pH 8.0), and 2 mM DTT. Images of frozen-hydrated Arp2/3 complex labeled with nanogold-labeled WA were recorded in focal pairs at 0.5 and 2.5 μm defocus using low-dose conditions. The position of the gold label within the reconstruction was calculated by backprojection from 10 class averages of gold-decorated particles (generated by superposition of the focal-pair images) after alignment to projections calculated from the undecorated reconstruction.
14. The budding yeast *Saccharomyces cerevisiae* Arp2/3 complex was purified as described (30). Bee1-WA, the 125 COOH-terminal residues of yeast Beep1 was purified as described (31, 32). Phalloidin-stabilized actin filaments were incubated with 25 nM Arp2/3 complex and 50 nM Bee1-WA domain in UBA buffer [50 mM Hepes (pH 7.5), 100 mM KCl, 3 mM MgCl₂, 1 mM EGTA, 0.2 mM ATP] for 5 min at 22°C. The pellet containing actin filaments and attached complexes was resuspended in UBA buffer and applied to copper grids coated with triafol holey carbon films (pelleting: Beckman-Coulter TLA-100 rotor at 70,000 rpm for 10 min at 4°C). The samples were stained with aqueous uranyl acetate, air-dried, and imaged at 2 μm defocus. The yeast data set consisted of 1157 particles selected from 13 images, and was processed following the procedure described for *Acanthamoeba* (11), which yielded a reconstruction very similar to that of *Acanthamoeba* (Fig. 1D).
15. R. D. Mullins, W. F. Stafford, T. D. Pollard, *J. Cell Biol.* **136**, 331 (1997).
16. Actin was isolated from rabbit skeletal muscle acetone powder (33) and further purified by gel filtration on Sephacryl S-300 in Ca-G buffer (22). Branches were prepared by polymerizing 4 μM Mg-ATP actin in the presence of 50 nM Arp2/3 and 200 nM Scar WA in Mg-G buffer [2 mM imidazole (pH 7.0), 200 μM ATP, 100 μM MgCl₂, 500 μM DTT] containing 1 × KMEI [50 mM KCl, 100 μM MgCl₂, 1 mM EGTA, 10

mM imidazole (pH 7.0)] for 2 min at 22°C followed by addition of 4 μM phalloidin 1 min before application to the Quantifoil grids. For the reconstruction of the branch junction, 167 clearly visible branches were interactively selected from 127 images. A reference-free alignment of these images gave class averages with branch angles of ~70°. The class with the clearest definition of actin monomers in the filaments was selected for reference-based alignment. To overcome the blurring of details due to small differences in branching angles, we generated three references emphasizing different portions of the structure. One reference focused on the mother filament, one on the daughter filament, and one on the central density of the branch junction. The complete data set was aligned to each of the references. Independent 2D averages were calculated and then merged (Fig. 2B). Atomic models of actin filaments (19) were fitted to the projection density of the mother and daughter filaments using COAN (29).

17. For myosin decoration, actin filaments were polymerized in the presence of Arp2/3 complex (25 nM) and Bee1-WA domain (50 nM) in UBA buffer (32). Samples were applied to the triafol grids and incubated with expressed smooth muscle myosin catalytic domain (no light chains) (34) prior to staining.
18. T. M. Svitkina, A. B. Verkhovsky, K. M. McQuade, G. G. Borisy, *J. Cell Biol.* **139**, 397 (1997).
19. M. Lorenz, D. Popp, K. C. Holmes, *J. Mol. Biol.* **234**, 826 (1993).
20. H. N. Higgs, T. D. Pollard, *J. Biol. Chem.* **274**, 32531 (1999).
21. D. C. Winter, E. Y. Choe, R. Li, *Proc. Natl. Acad. Sci. U.S.A.* **96**, 7288 (1999).

22. K. J. Amann, T. D. Pollard, *Nature Cell Biol.* **3**, 306 (2001).
23. D. Pantaloni, R. Boujemaa, D. Didry, P. Gounon, M. F. Carlier, *Nature Cell Biol.* **2**, 385 (2000).
24. L. M. Machesky, R. H. Insall, *Curr. Biol.* **8**, 1347 (1998).
25. L. Blanchoin *et al.*, *Nature* **404**, 1007 (2000).
26. L. M. Machesky, S. J. Atkinson, C. Ampe, J. Vandekerckhove, T. D. Pollard, *J. Cell Biol.* **127**, 107 (1994).
27. M. Way, J. Gooch, B. Pope, A. G. Weeds, *J. Cell Biol.* **109**, 593 (1989).
28. S. J. Ludtke, P. R. Baldwin, W. Chiu, *J. Struct. Biol.* **128**, 82 (1999).
29. N. Volkmann, D. Hanein, *J. Struct. Biol.* **125**, 176 (1999).
30. D. Winter, A. V. Podtelejnikov, M. Mann, R. Li, *Curr. Biol.* **7**, 519 (1997).
31. R. Li, *J. Cell Biol.* **136**, 649 (1997).
32. D. Winter, T. Lechler, R. Li, *Curr. Biol.* **9**, 501 (1999).
33. J. A. Spudich, S. Watt, *J. Biol. Chem.* **246**, 4866 (1971).
34. K. M. Trybus, *J. Biol. Chem.* **269**, 20819 (1994).
35. We are grateful to G. Ouyang for technical assistance, to K. M. Trybus and S. Lowey for the myosin sample, to S. Almo for critical reading of the manuscript, and to R. Liddington for helpful discussions and valuable comments on the manuscript. Supported by NIH research grants (T.D.P., R.L.), an NIH postdoctoral fellowship (K.J.A.), and the Human Frontier Science Program (C.E.). D.H. is a Pew Scholar in the Biomedical Sciences.

31 May 2001; accepted 24 July 2001
 Published online 30 August 2001;
 10.1126/science.1063025
 Include this information when citing this paper.

Trans-Suppression of Misfolding in an Amyloid Disease

Per Hammarström, Frank Schneider, Jeffery W. Kelly*

The transthyretin (TTR) amyloid diseases, representative of numerous misfolding disorders, are of considerable interest because there are mutations that cause or suppress disease. The Val³⁰ → Met³⁰ (V30M) TTR mutation is the most prevalent cause of familial amyloid polyneuropathy in heterozygotes, whereas a Thr¹¹⁹ → Met¹¹⁹ (T119M) mutation on the second TTR allele protects V30M carriers from disease. Here, we show that the incorporation of one or more T119M TTR subunits into a predominantly V30M tetramer strongly stabilized the mixed tetramer against dissociation. Dissociation is required for amyloid formation, so these findings provide a molecular explanation for intragenic *trans*-suppression of amyloidosis. The data also suggest a potential therapeutic strategy, provide insight into tissue-specific deposition and amyloid composition, and support the validity of the amyloid hypothesis in human disease.

The amyloidoses are a large group of protein misfolding diseases (1–3). The 80 transthyretin (TTR) amyloid diseases are representative of those where a full-length protein composes the fibrils. The TTR familial amyloid polyneuropathy (FAP) mutations (e.g., V30M) make TTR more susceptible to dissociation and the conformational changes that enable amyloid deposition and pathology. Com-

pound heterozygotes having V30M and T119M TTR mutations on different alleles have few, if any, manifestations of FAP (4, 5), suggesting that the incorporation of a stabilizing subunit in an oligomeric protein such as TTR can protect against misfolding and disease. Previous studies document the increased stability of T119M-containing TTR and the decreased stability of the V30M-containing TTR, relative to the wild type (WT) (6–8).

Here, we evaluate the amyloidogenicity and stability of individual tetramers with defined V30M and/or T119M subunit composition to explain the T119M *trans*-suppression that protects compound heterozygotes from disease.

Department of Chemistry and The Skaggs Institute of Chemical Biology, The Scripps Research Institute, 10550 North Torrey Pines Road BCC265, La Jolla, CA 92037, USA.

*To whom correspondence should be addressed. E-mail: jkelly@scripps.edu